Supplementary Information

Exploring Artificially Induced Nonstoichiometric Effect of Li_2RuO_3 as Reactive Promoter on Electrocatalytic Behavior

Haeseong Jang[‡a], Wooyoung Jin[‡a], Gyutae Nam[ab], Youngshin Yoo[a], Jeong Suk Jeon[c], Joohyuk Park*[ad], Min Gyu Kim *[c], and Jaephil Cho*[a]

[a]Department of Energy Engineering, School of Energy and Chemical Engineering, Ulsan National Institute of Science and Technology (UNIST), 50, UNIST-gil, Ulsan 44919, Republic of Korea

[b]Present address: School of Materials Science and Engineering, Georgia Institute of Technology, Atlanta, Georgia 30332-0245, USA

[c]Beamline Research Division, Pohang Accelerator Laboratory, Pohang University of Science and Technology, Pohang, 790-784, South Korea

[d]Present address: Department of Materials, University of Oxford, Parks Road, Oxford OX1 3PH, United Kingdom

***e-mail:** joohyuk.park@materials.ox.ac.uk; mgkim@postech.ac.kr; jpcho@unist.ac.kr

[‡]Theses authors contributed equally to this work.

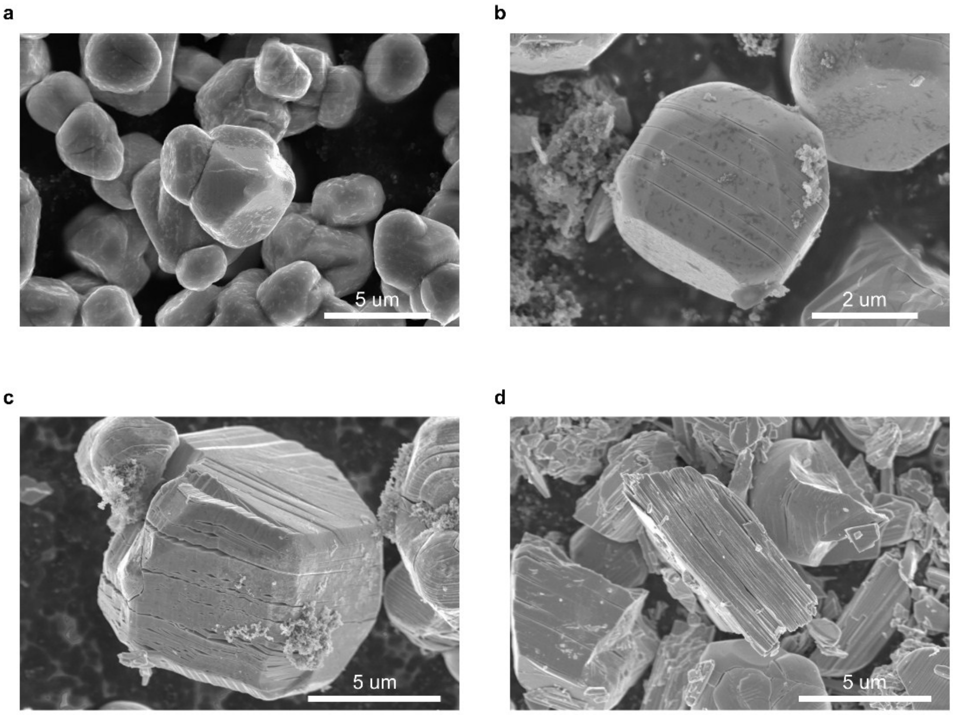

Fig. S1 Scanning electronic microscopy (SEM) images. SEM images of the (**a**) LRO, (**b**) 3.6V-LRO, (**c**) 4.3V-LRO, and (**d**) 5.0V-LRO.

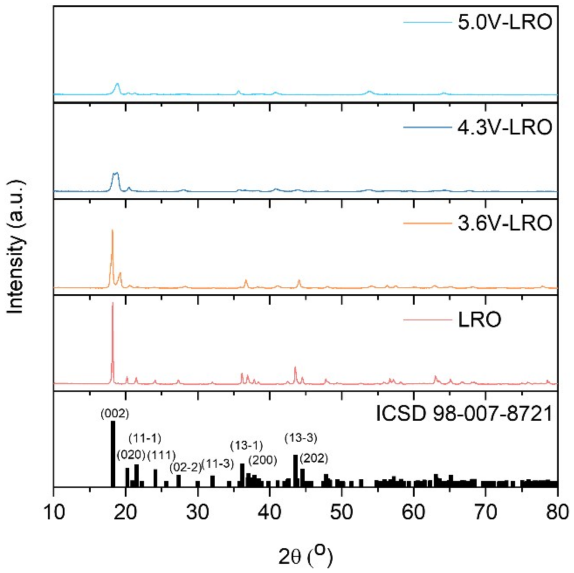

Fig. S2 XRD patterns of LRO series. As the delitiation process proceeds, the overall XRD peaks of the $Li_{2-x}RuO_3$ series become broader and the intensity decreases, indicating a decrease in crystallinity of the structure. In addition, in the xrd pattern, the Full Width at Half Maximum (FWHM), which is closely related to the lattice strain and the crystallite size of the particles, was reduced. In particular, when 3.6V-LRO is charged from 4.3V-LRO, the excessive collapse of peaks occurs, which is an area where oxygen gas is generated and the oxygen network is modified due to oxidation of oxygen. The collapse of the (002) mono peak coincides with the tendency of intragranular cracks in the {111} cubic direction in Figure 1d-f.

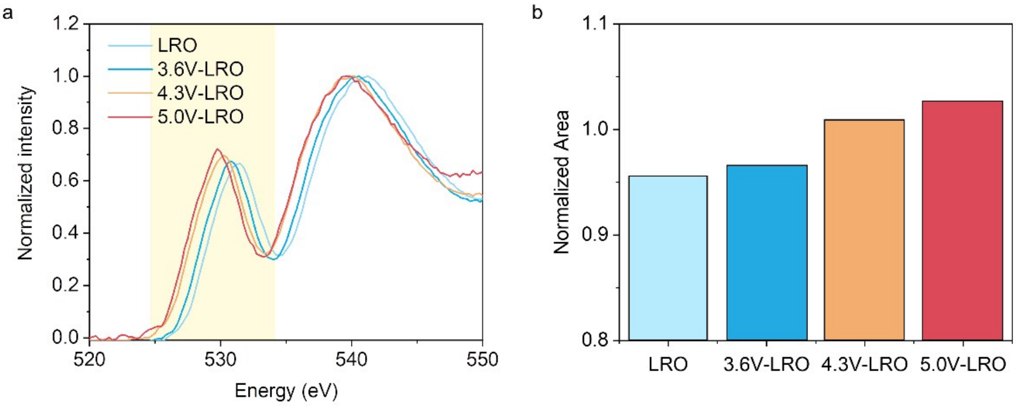

Fig. S3 a, O K-edge EELS spectra of $Li_{2-x}RuO_{3-y}$ series. The 530 eV region, shown in yellow, is the pre-edge region of the oxygen K-edge, indicating the hybridization state of TM3d-O2p. The integral value of the pre-edge peak is directly related to the degree of TM3d-O2p hybridization, and the bar graph **b,** represents the degree of TM-O hybridization according to the material.

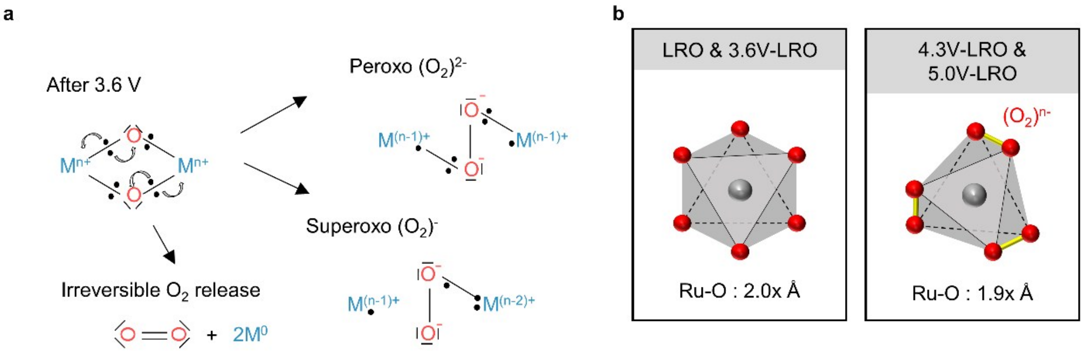

Fig. S4 a, Schematic illustration of oxygen network modification in the oxygen redox region. After 3.6 V, oxidation of peroxo-like species (peroxo $(O_2)^{2-}$, superoxo $(O_2)^{-}$), and irreversible O_2 release occur during reversible and irreversible oxygen redox, resulting in formation of O-O bonds and modification of oxygen network. **b**, Visualization of peroxo-like species upon delithiation.

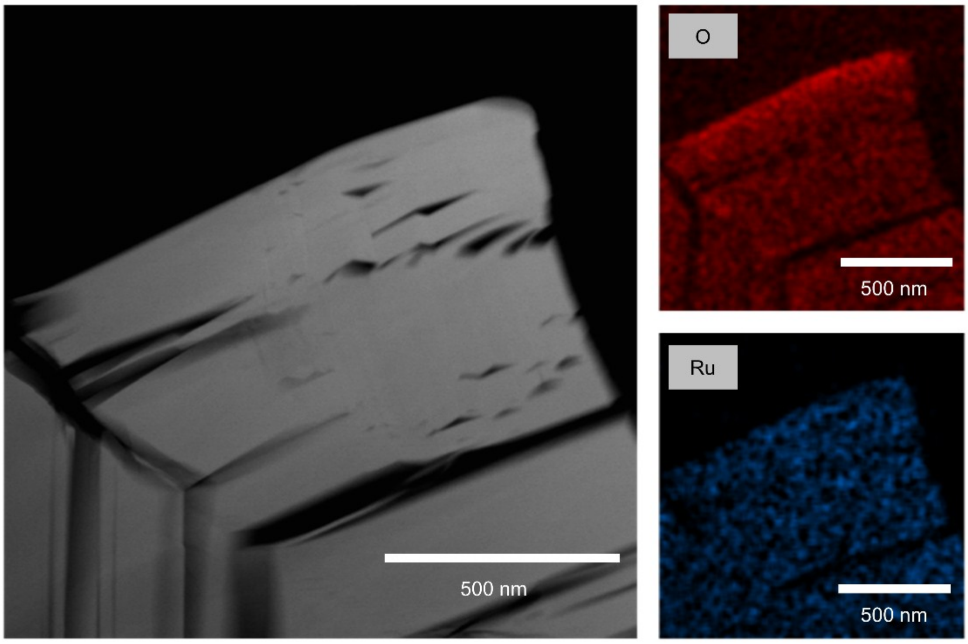

Fig. S5 STEM images of 5.0V-LRO with elemental mappings of Ru and O through EDS

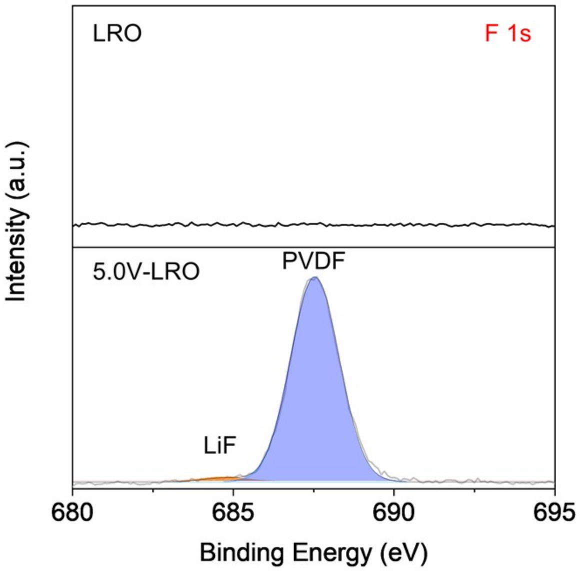

Fig. S6 Fluorine 1s X-ray photoelectron spectroscopy (XPS) spectra of LRO and 5.0V-LRO. There were two peaks at binding energies of 684.9 eV (LiF) and 687.7 eV (PVDF) in 5.0V-LRO, while there is no obvious peak in LRO. It implied that 5.0V-LRO has thin CEI.

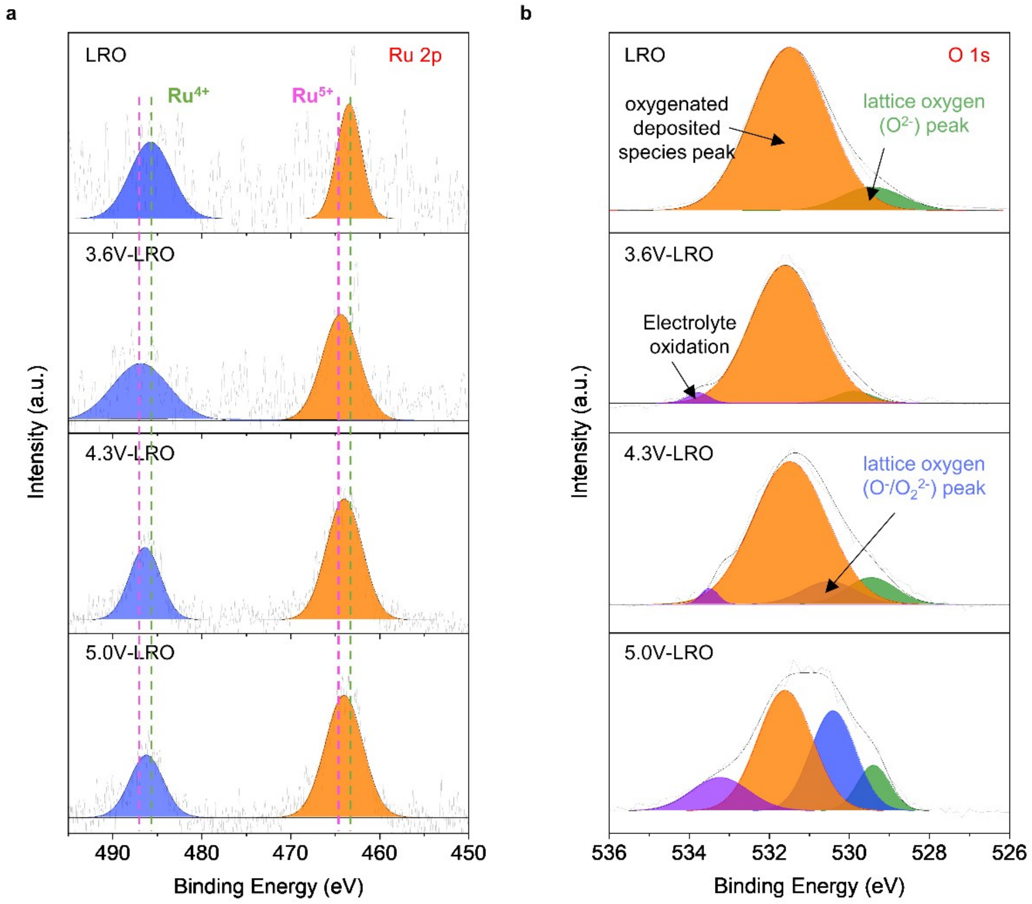

Fig. S7 XPS of Ru 3p and O 1s in $Li_{2-x}RuO_{3-y}$ series. a) LRO, b) 3.6V-LRO, c) 4.3V-LRO, and d) 5.0V-LRO. Because of the spin orbital coupling, the Ru 3p spectrum is separated into $3p_{3/2}$ components located at 465 eV and $3p_{1/2}$ components at 486 eV. The peak shift of 3.6V-LRO to ~0.8 eV occurred because the oxidation number of ruthenium increased from 4+ to 5+. Interestingly, in the 4.3V-LRO and 5.0V-LRO, a shift in the low binding energy (~0.4 eV) occurred. The O 1s spectra shows two peaks characteristic of lattice oxygen (O^{2-}) and oxygenated deposited. In the process of Li extraction from LRO to 3.6V-LRO, there was barely change, but notable changes from 4.3V-LRO and 5.0V-LRO.

Table S1 inductively coupled plasma-optical emission spectroscopy (ICP-OES) results. The amounts of delithiation were calculated assuming no loss of Ru ions

Sample	LRO	3.6V-LRO	4.3V-LRO	5.0V-LRO
Expected Composition	Li_2RuO_3	$Li_{1.21}RuO_3$	$Li_{0.52}RuO_{3-\beta}$	$Li_{0.15}RuO_{3-\delta}$

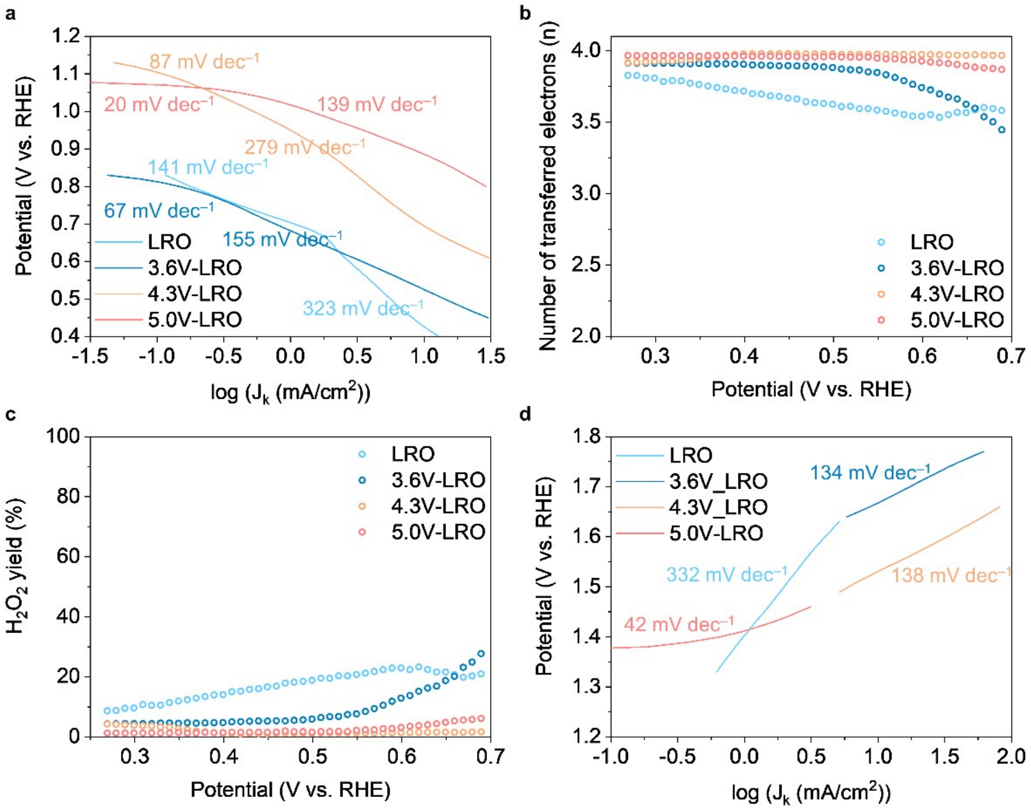

Fig. S8 Electrochemical characteristic. **a, d,** The corresponding Tafel plots of LRO, 3.6V-LRO, 4.3V-LRO, and 5.0V-LRO (**a**) for ORR and (**d**) for OER. **b,** Corresponding Number of transferred electrons LRO, 3.6V-LRO, 4.3V-LRO, and 5.0V-LRO. **c,** Corresponding hydrogen peroxide yield of LRO, 3.6V-LRO, 4.3V-LRO, and 5.0V-LRO.

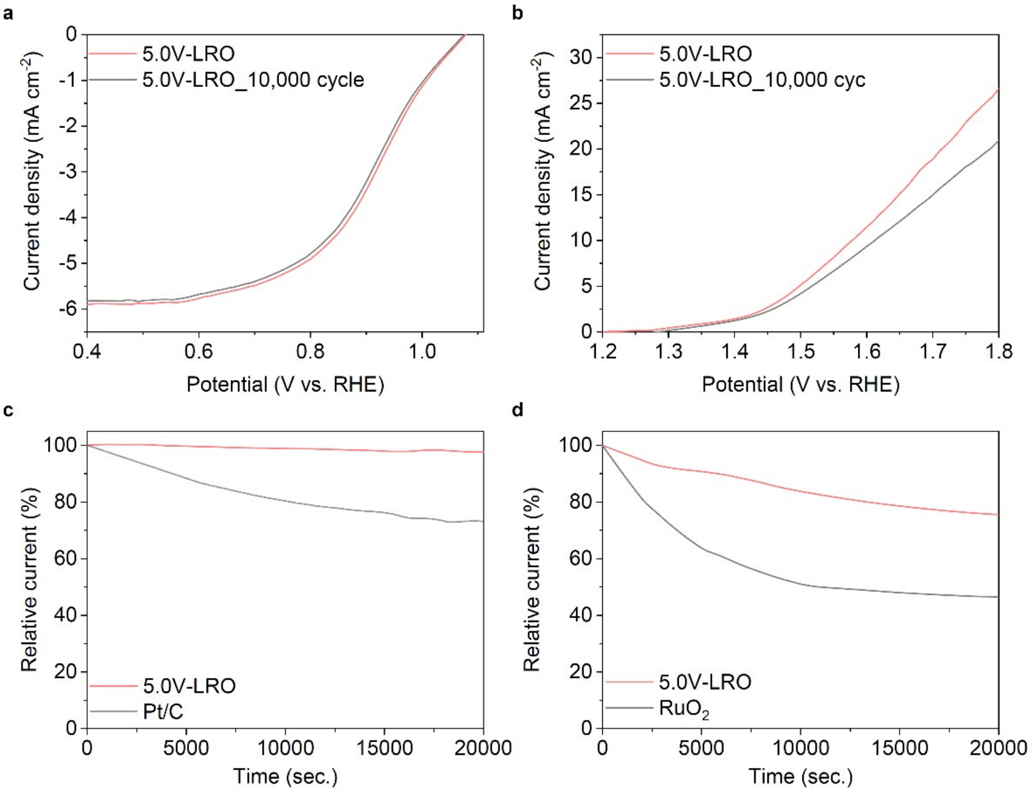

Fig. S9 a, b, Durability test of 5.0V-LRO by measuring linear sweep voltammetry after 10,000 cycling for (**a**) ORR and (**b**) OER at a scan rate of 20 mV s^{-1}. **c,d,** Chronoamperometric response of the reference samples (Pt/C or RuO$_2$) and 5.0V-LRO in O$_2$-saturated 0.1 M KOH electrolytes with 1600 r.p.m for (**c**) ORR at 0.4 V (vs. RHE) (**d**) OER at voltage where current density is 10 mA cm^{-2}.

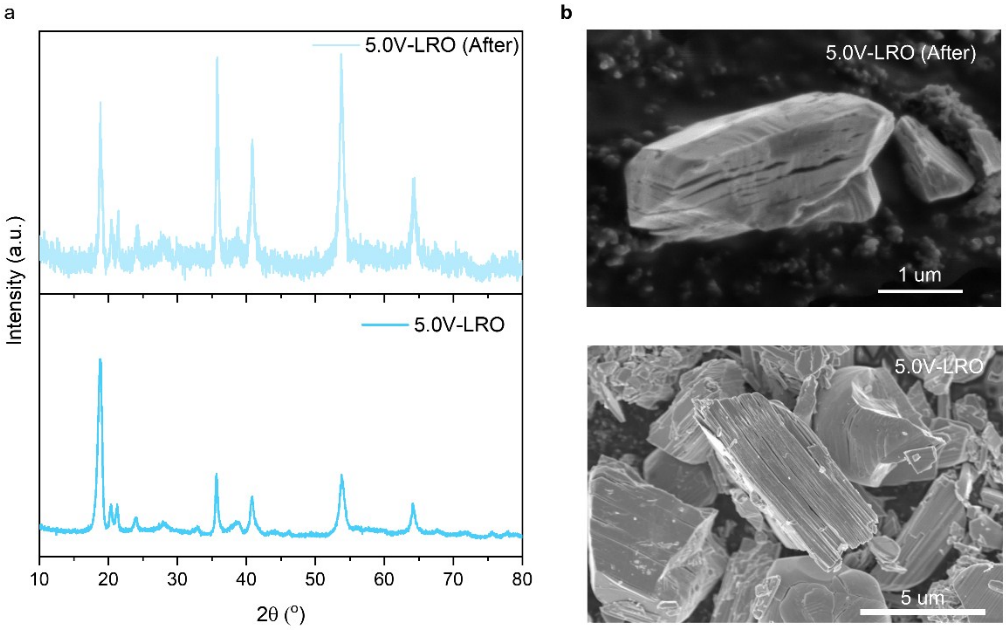

Fig. S10 a, XRD results and **b,** SEM images of 5.0V-LRO and 5.0V-LRO after stability test.

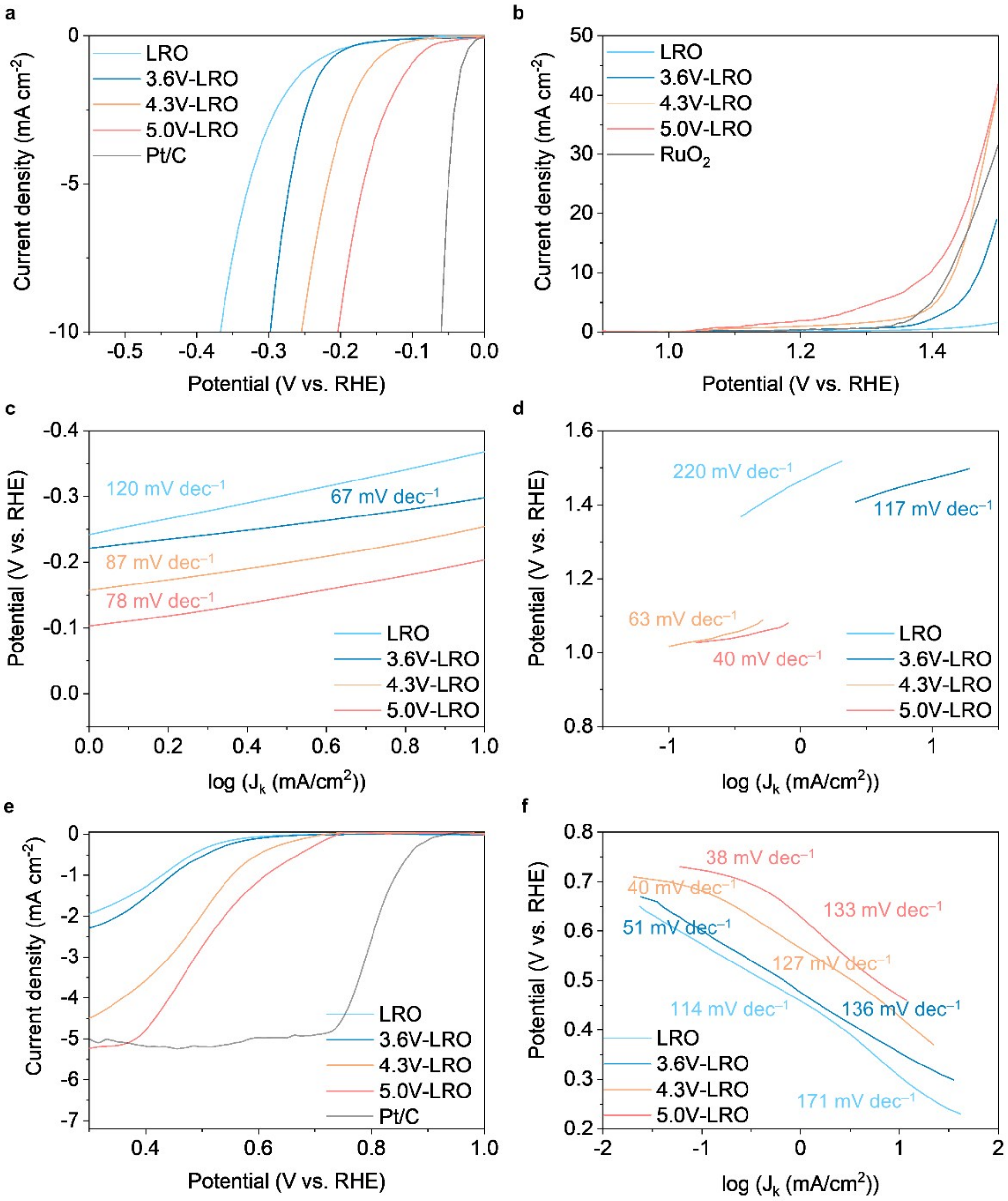

Fig. S11 Hydrogen evolution reaction (HER), Oxygen evolution reaction (OER), and Oxygen reduction reaction (ORR) performance. **a,b,e,** polarization curves and linear sweep voltammetry (LSV) curves of LRO, 3.6V-LRO, 4.3V-LRO, 5.0V-LRO, and reference samples (Pt/C or RuO$_2$) in 0.5 M H_2SO_4 electrolyte at a scan rate of 10 mV s^{-1} (**a**) for HER, (**b**) for OER, and (**e**) for ORR. **c,d,f,** The corresponding Tafel plots of LRO, 3.6V-LRO, 4.3V-LRO, and 5.0V-LRO (**a**) for HER, (**d**) for OER, and (**f**) for ORR.

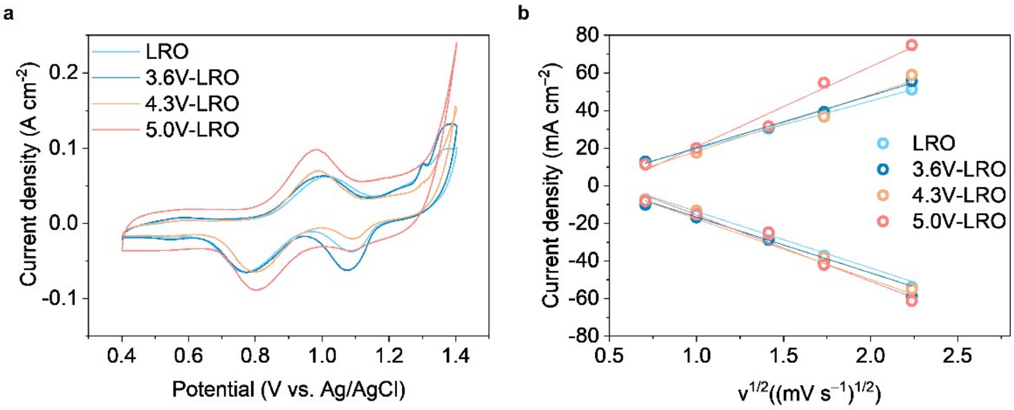

Fig. S12 VO^{2+}/VO_2^+ half-cell reactions. **a,** Cyclic voltammograms (CVs) of of LRO, 3.6V-LRO, 4.3V-LRO, and 5.0V-LRO at a scan rate of 5 mV s^{-1} with the potential window of 0.4 to 1.3 V versus Ag/AgCl in 0.1 M $VOSO_4$ + 3 M H_2SO_4 solutions. **b,** Randles-Sevcik plot obtained from the CV data

Table S2 Summary of Cyclic voltammetry results.

$V^{4+} \leftrightarrow V^{5+}$	E_{pa} (V)	E_{pc} (V)	ΔE (V)	I_{pa} (A cm^{-2})	I_{pc} (A cm^{-2})	I_{pa}/I_{pc}
LRO	1.014	0.773	0.241	0.0631	0.0658	0.95
3.6V-LRO	1.003	0.774	0.229	0.0640	0.0660	0.97
4.3V-LRO	0.984	0.838	0.171	0.0697	0.0650	1.07
5.0V-LRO	0.977	0.811	0.166	0.0976	0.0884	1.10

Table S3 Electrical conductivity and resistivity of the electrocatalyst-loaded air electrodes.

Sample	Air-electrode	LRO	3.6V-LRO	4.3V-LRO	5.0V-LRO
Conductivity ($S\ cm^{-1}$)	3.19×10^{-2}	3.36×10^{-2}	3.62×10^{-2}	3.55×10^{-2}	3.47×10^{-2}
Resistivity (Ω cm)	31.3	29.8	27.6	28.2	28.8

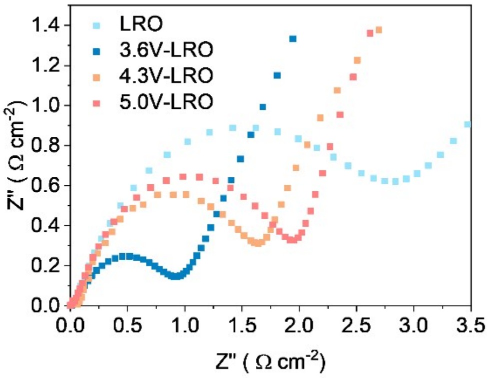

Fig. S13 Electrochemical impedance spectroscopy (EIS) results of LRO LRO, 3.6V-LRO, 4.3V-LRO, and 5.0V-LRO.

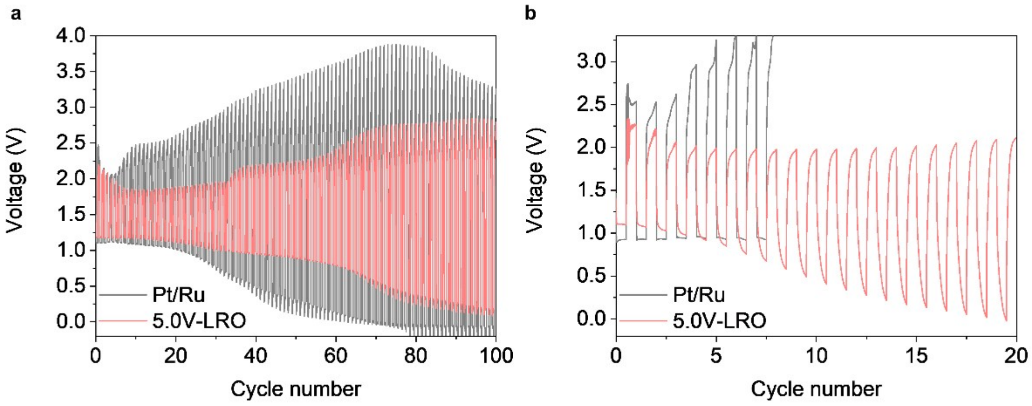

Fig. S14 Rechargeable Zinc-air batteries (ZAB) cycling profiles. **a,b,** Rechargeable ZAB cycling profiles at (dis)charge current density of (**a**) 20 mA cm^{-2} (**b**) 50 mA cm^{-2} (20 min per cycle).

Table S4 summary and comparison of the Zn-air battery performances.

Catalyst	Electrolyte	OCV (V)	Peak power density (mW cm^{-2})	Current density (mA cm^{-2})	Discharge time (min)	Specific capacity (mAh g^{-1})	Gravimetric energy density (Wh kg^{-1})	Cycle time, Overpotential
5V-LRO (This work)	**6 M KOH**	**1.53**	**328.1**	**10**	-	-	-	**33.3 h, 0.7 V**
				20	-	-	-	**33.3 h, -**
				50	**67 (Static)**	**360.1**	**395.3**	**6.67 h, -**
					220 (Flow)	**917.2**	**875.2**	
Pt-SCFP/C-12[1]	6 M KOH + 0.2 N $ZnCl_2$	1.44	122	5	-	790.4	-	80h, 0.86 V
				10		781.5		-
Co_3Ni_2/CN (st)[2]	6 M KOH	1.48	331	50	-	730	-	-
5rG@NHCS[3]	6 M KOH	1.54	142	50	600		-	-
				100	300	670		

Fe2P/NPC[4]	6 M KOH + 0.2 M $Zn(CH_3COO)_2$	1.469	111.6	10	-	654.1	733.6	-
SA-Fe/N/C-20-900[5]	6 M KOH + 0.2 M $Zn(CH_3COO)_2$	1.34	22.2	5	-	-	927.9	10 h, 0.9 V
FeNi/HNC[6]	6 M KOH	1.43	310	10	1,920	-	-	24 h, 0.8 V
				50	960	-	-	
FeCo@MNC[7]	6 M KOH + 0.2 M $Zn(CH_3COO)_2$	1.41	115	20	-	-	-	24.2 h, 0.9 V
Fe-N_x-C[8]	6 M KOH + 0.2 M $Zn(CH_3COO)_2$	1.51	96.4	5	-	-	-	300 h, 0.988 V
				10	2000	641	-	250 h, 1.255 V
T-CoNCNTs//NiFe-LDH arrays[9]	6 M KOH + 0.2 M $Zn(CH_3COO)_2$	1.39	245	50	-	-	-	33.3 h, 0.9 V
CNCo-600[10]	6 M KOH + 0.2 M $Zn(CH_3COO)_2$	-	479.1	5	-	-	-	33.3 h, 0.75 V

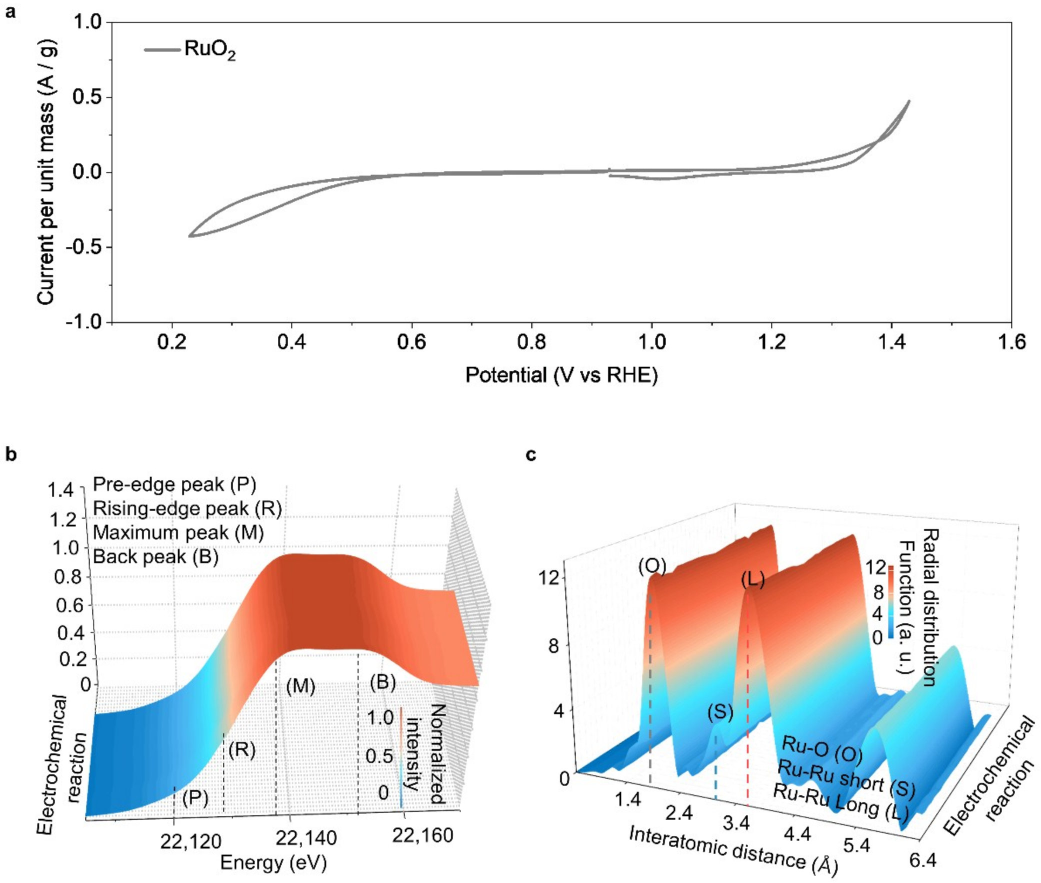

Fig. S15 *Operando* X-ray absorption spectroscopy (XAS) analysis results of RuO$_2$. **a,** Obtained CV profile during *Operando* XAS of RuO$_2$. Corresponding representative **b,** *Operando* XANES profile of Ru K-edge. The three main peaks, denoted by the dotted lines, are labeled as rising peak (R), maximum peak (M), and back peak (B). **c,** *Operando* RDF of Fourier-transformed k^3-weighted EXAFS spectra of Ru K-edge. The three main bonds, Ru-O bond (Ru$_{\text{-O}}$), Ru-Ru short bond (Ru-Ru$_{\text{-short}}$), and Ru-Ru long bond (Ru-Ru$_{\text{-long}}$), are labeled as O, S, and L.

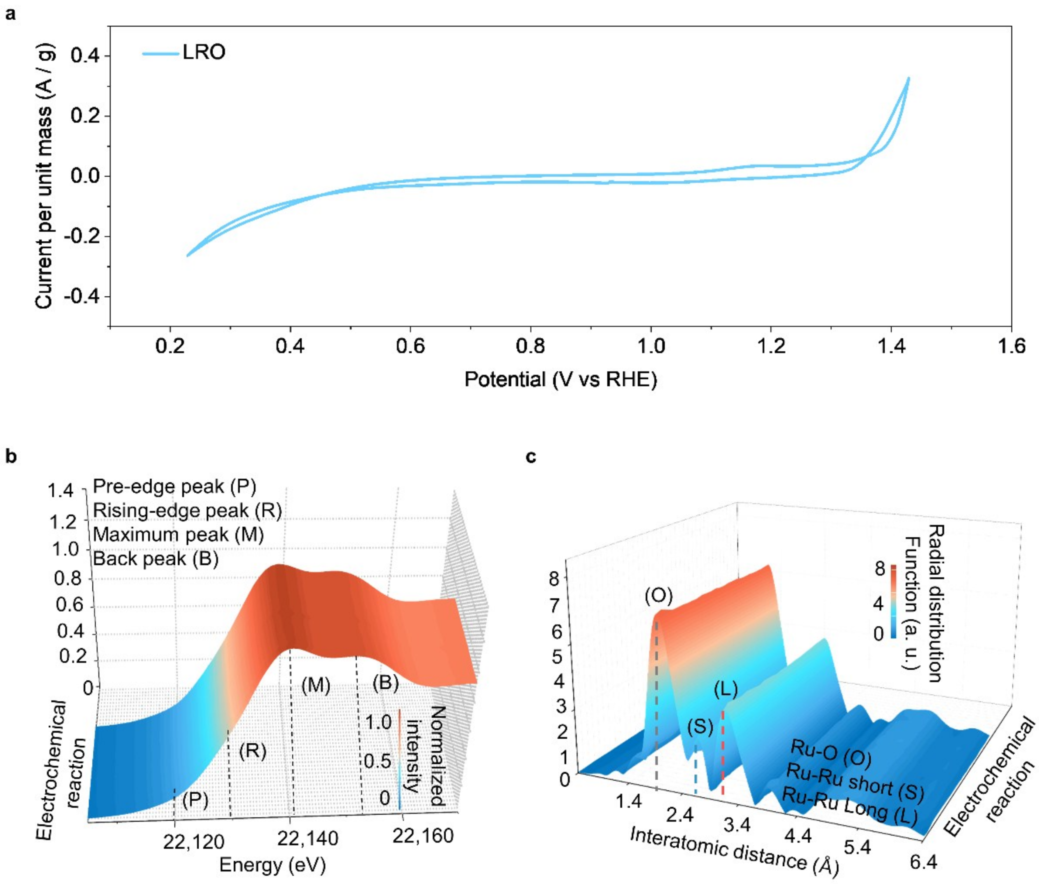

Fig. S16 *Operando* X-ray absorption spectroscopy (XAS) analysis results of LRO. **a,** Obtained CV profile during *Operando* XAS of LRO. Corresponding representative **b,** *Operando* XANES profile of Ru K-edge. The three main peaks, denoted by the dotted lines, are labeled as Rising peak (R), Maximum peak (M), and Back peak (B). **c,** *Operando* RDF of Fourier-transformed k^3-weighted EXAFS spectra of Ru K-edge. The three main bonds, Ru-O bond (Ru_{-O}), Ru-Ru short bond ($Ru\text{-}Ru_{-short}$), and Ru-Ru long bond ($Ru\text{-}Ru_{-long}$), are labeled as O, S, and L.

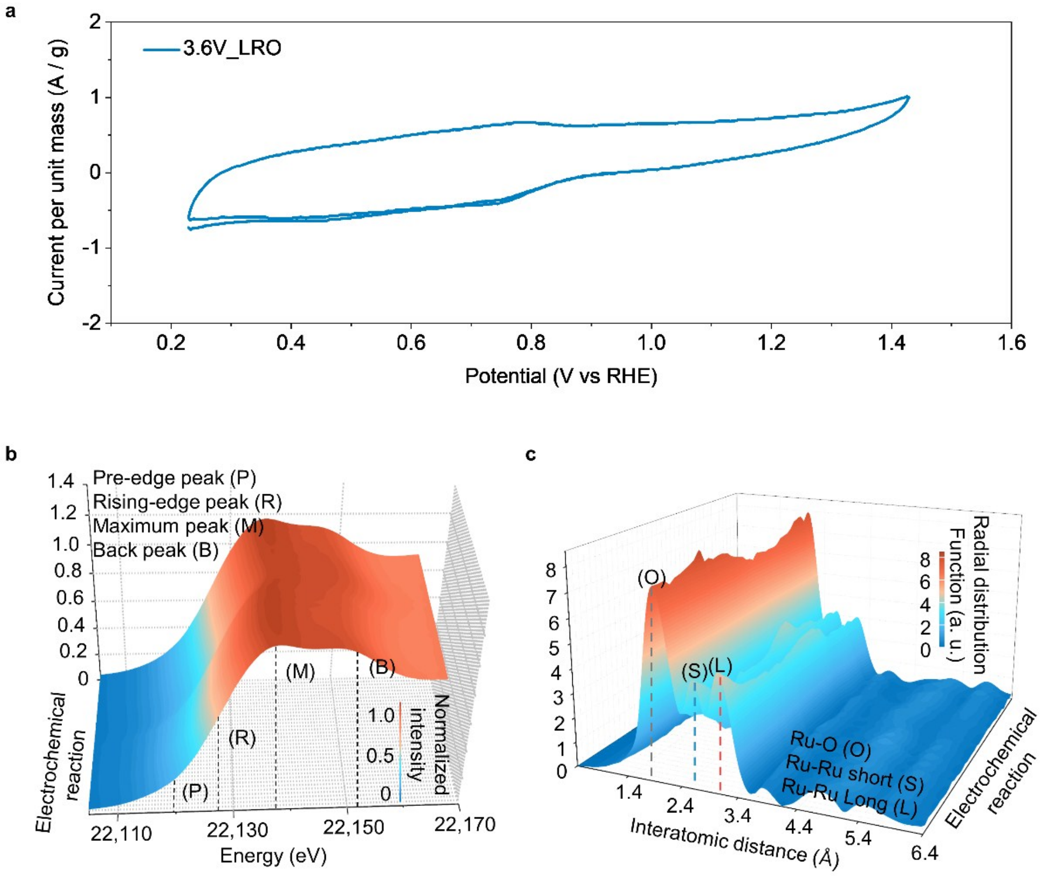

Fig. S17 *Operando* X-ray absorption spectroscopy (XAS) analysis results of 3.6V-LRO. **a,** Obtained CV profile during *Operando* XAS of 3.6V-LRO. Corresponding representative **b,** *Operando* XANES profile of Ru K-edge. The three main peaks, denoted by the dotted lines, are labeled as rising peak (R), maximum peak (M), and back peak (B). **c,** *Operando* RDF of Fourier-transformed k^3-weighted EXAFS spectra of Ru K-edge. The three main bonds, Ru-O bond (Ru$_{\text{-O}}$), Ru-Ru short bond (Ru-Ru$_{\text{-short}}$), and Ru-Ru long bond (Ru-Ru$_{\text{-long}}$), are labeled as O, S, and L.

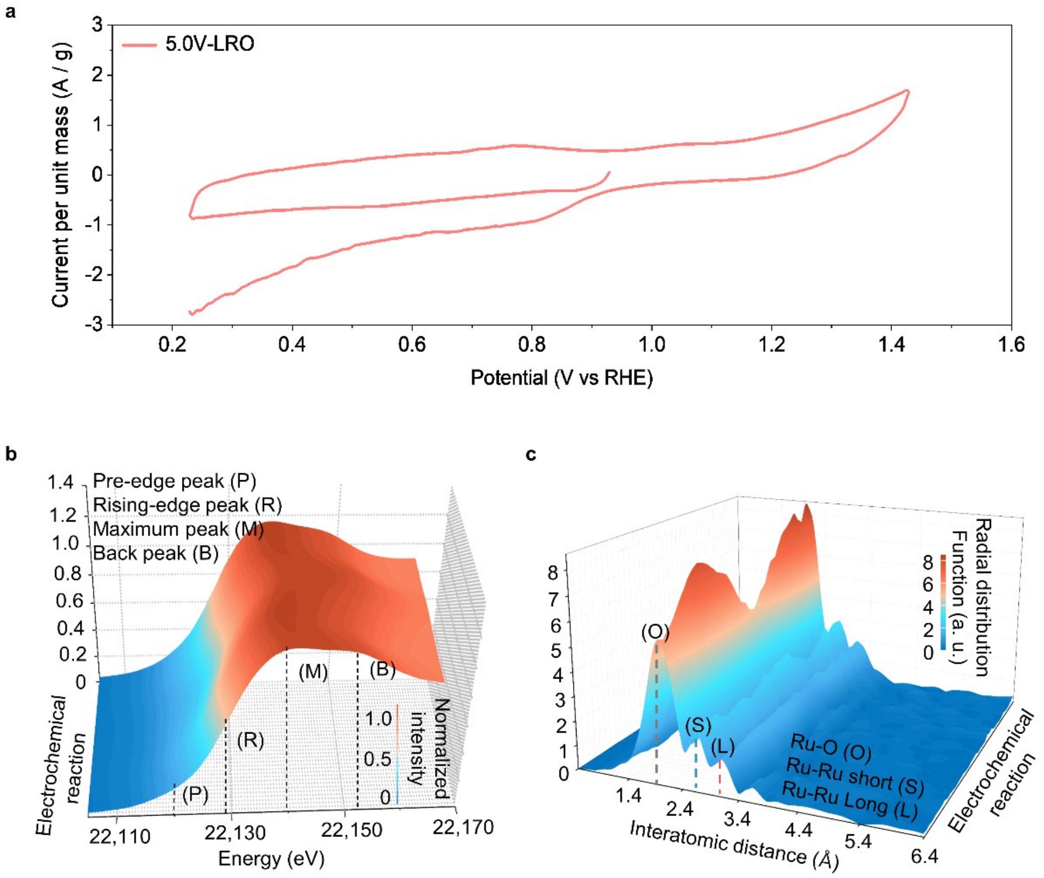

Fig. S18 *Operando* X-ray absorption spectroscopy (XAS) analysis results of 5.0V-LRO. **a,** Obtained CV profile during *Operando* XAS of 5.0V-LRO. Corresponding representative **b,** *Operando* XANES profile of Ru K-edge. The three main peaks, denoted by the dotted lines, are labeled as rising peak (R), maximum peak (M), and back peak (B). **c,** *Operando* RDF of Fourier-transformed k^3-weighted EXAFS spectra of Ru K-edge. The three main bonds, Ru-O bond (Ru$_{\text{-O}}$), Ru-Ru short bond (Ru-Ru$_{\text{-short}}$), and Ru-Ru long bond (Ru-Ru$_{\text{-long}}$), are labeled as O, S, and L.

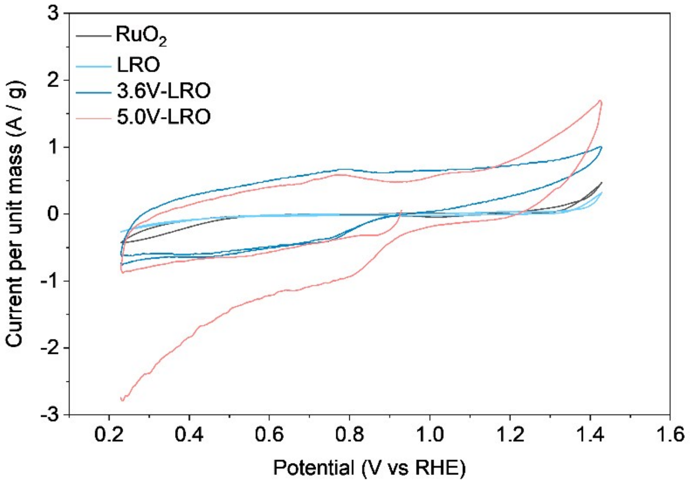

Fig. S19 Comparison of obtained CV profile during Operando XAS of RuO$_2$, LRO, 3.6V-LRO, and 5.0V-LRO

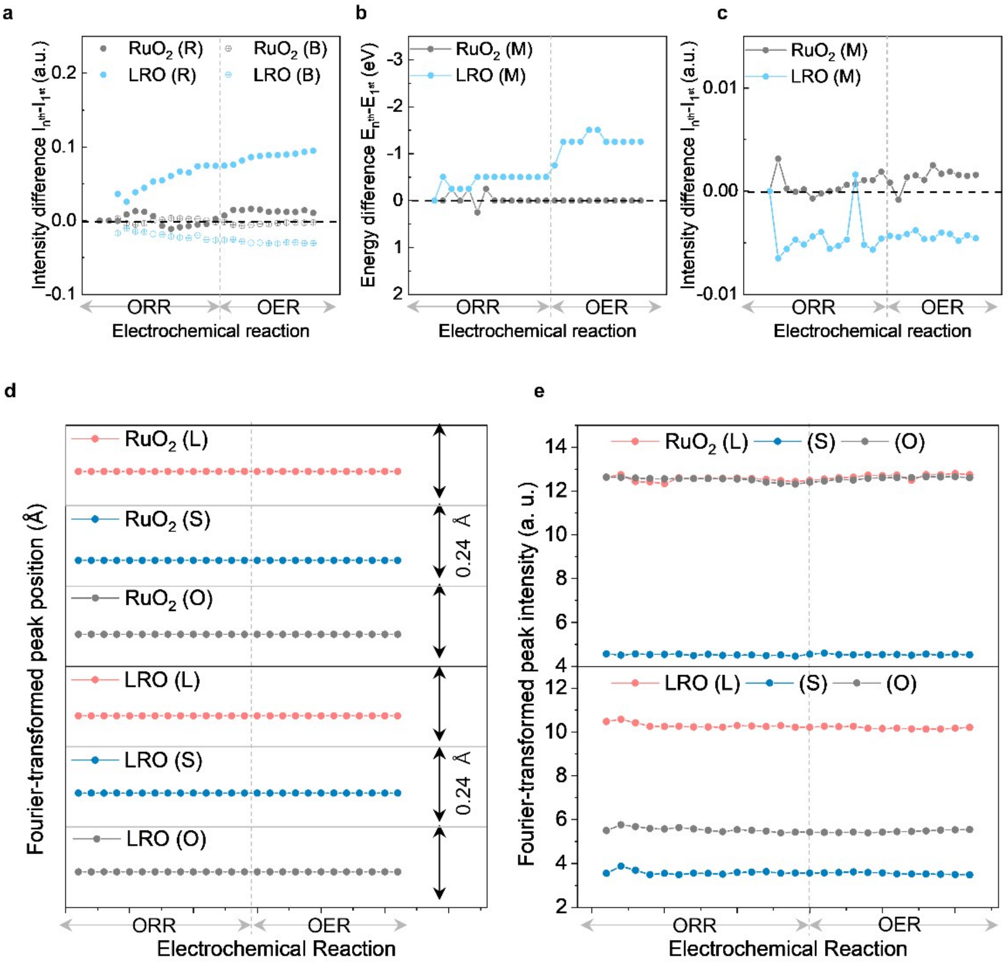

Fig. S20 Summary of *Operando* Ru K-edge XANES spectrum and EXAFS spectrum. **a,c,** The normalized intensity difference Ru K-edge XANES spectra (ΔI : $I_{n^{th}} - I_{1^{st}}$) of (**a**) Rising peak (R) and Back peak (B) cross line and (**c**) Maximum peak (M) cross line in RuO_2 and LRO. **b,** the photon energy change ($E_{n^{th}} - E_{1^{st}}$) of Maximum peak (M) in RuO_2 and LRO. **d,e,** (**d**) The Fourier-transformed (FT) peak position change and (**e**) the FT peak intensity change of RuO_2 and LRO. Ru-O bond (Ru$_{\text{-O}}$, ~2.04 Å), Ru-Ru short bond (Ru-Ru$_{\text{-short}}$, ~2.52 Å), and Ru-Ru long bond (Ru-Ru$_{\text{-long}}$, ~2.75 Å) are labeled as O, S, and L.

Reference

1. X. Wang, J. Sunarso, Q. Lu, Z. Zhou, J. Dai, D. Guan, W. Zhou and Z. Shao, *Advanced Energy Materials*, 2020, **10**, 1903271.
2. X. Yang, Q. Yi, K. Sheng and T. Wang, *Catalysis Letters*, 2020, DOI: 10.1007/s10562-020-03198-9.
3. K. Sheng, Q. Yi, L. Hou and A. Chen, *Journal of The Electrochemical Society*, 2020, **167**, 070560.
4. L. Chen, Y. Zhang, L. Dong, X. Liu, L. Long, S. Wang, C. Liu, S. Dong and J. Jia, *Carbon*, 2020, **158**, 885-892.
5. D. Chen, J. Ji, Z. Jiang, M. Ling, Z. Jiang and X. Peng, *Journal of Power Sources*, 2020, **450**, 227660.
6. H. Wu, M. Zeng, Z. Li, X. Zhu, C. Tian, C. Xia, L. He and S. Dai, *Sustainable Energy & Fuels*, 2019, **3**, 136-141.
7. C. Li, M. Wu and R. Liu, *Applied Catalysis B: Environmental*, 2019, **244**, 150-158.
8. J. Han, X. Meng, L. Lu, J. Bian, Z. Li and C. Sun, *Advanced Functional Materials*, 2019, **29**, 1808872.
9. W. Xu, Z. Lu, T. Zhang, Y. Zhong, Y. Wu, G. Zhang, J. Liu, H. Wang and X. Sun, *Energy Storage Materials*, 2019, **17**, 358-365.
10. C. You, X. Gao, Q. Wang, X. Li, S. Tan, P. Xu, D. Cai, Y. Weng, C. Wang, X. Tian and S. Liao, *ACS Applied Materials & Interfaces*, 2019, **11**, 44153-44160.